# Lattice Dynamics of $Cu_2ZnSn(S_x,Se_{1-x})_4$ Kesterite Thin-Film Solar Cells Studied by Nuclear Inelastic Scattering

*Raju Edla[a*], David Nowak[b], Dirk Hauschild[a, c, d], Ilya Sergueev[e], Devendra Pareek[b], Levent Gütay[b], Clemens Heske[a, c, d], Lothar Weinhardt[a, c, d], and Svetoslav Stankov[a, f*]*

[a]Institute for Photon Science and Synchrotron Radiation (IPS), Karlsruhe Institute of Technology (KIT), Karlsruhe, Germany

[b]Ultrafast Nanoscale Dynamics, Institute of Physics, Carl von Ossietzky University of Oldenburg, Oldenburg, Germany

[c]Institute for Chemical Technology and Polymer Chemistry (ITCP), Karlsruhe Institute of Technology (KIT), Karlsruhe, Germany

[d]Department of Chemistry and Biochemistry, University of Nevada, Las Vegas (UNLV), Las Vegas, USA

[e]Deutsches Elektronen-Synchrotron DESY, Hamburg, Germany

[f]Laboratory for Applications of Synchrotron Radiation (LAS), Karlsruhe Institute of Technology (KIT), Karlsruhe, Germany

*** Authors to whom correspondence should be addressed:**

edla.raju@kit.edu, s.stankov@kit.edu

**Keywords**: Kesterites, solar cells, defects, phonon density of states, nuclear inelastic scattering, *operando* measurements

**Abstract**

Phonons play a crucial role for thermalization and non-radiative recombination losses in semiconductors, impacting the power conversion efficiency (PCE) of solar cells. To shed light on the lattice dynamics in $Cu_2ZnSn(S_x,Se_{1-x})_4$ (CZTSSe) thin-film solar cells and validate the extensive number of theoretical studies, we determine the $^{119}$Sn-partial phonon density of states (Sn-PDOS) by nuclear inelastic X-ray scattering. CZTSSe-based devices, one with near-stoichiometric and two with off-stoichiometric compositions are investigated, and the results are correlated with the corresponding PCEs of 3.2, 7.6, and 10.6 %, respectively. Compared to the near-stoichiometric cell, the main Sn-PDOS peak of the off-stoichiometric cells broadens and slightly shifts to higher energy, this effect is correlated with the type and concentration of the characteristic defects in the studied samples. Furthermore, the Sn-PDOS of the 10.6 % device is also obtained under *operando* (maximum power point) and open-circuit conditions. A comparison of the Sn-PDOS before and after the *operando* measurements suggests structural changes, likely due to the formation of metastable defects. In agreement with the theoretical studies, the Sn-PDOS of CZTSSe absorber shows additional peaks compared to CZTSe attributed to coupling of Sn to the vibrations of Se and S atoms. This work paves the way for a further understanding of the lattice dynamics and subsequent enhancement of the PCEs of thin-film solar cells, as well as other applied materials and devices containing elements that are Mössbauer-active and hence suitable for Nuclear Inelastic Scattering.

## 1. Introduction

Efficient solar energy harvesting, via photovoltaic (PV) or photoelectrochemical water splitting (PEC) technologies, has the potential to help meet the continuously growing energy demand by providing green renewable energy[1]. Intense research efforts in the last decades have been devoted to optimizing the existing and discovering new materials and devices, which resulted in a dramatic increase of the power conversion efficiencies (PCEs)[2] across many different technologies. Devices with kesterite-based absorbers ($Cu_2ZnSn(S_x,Se_{1-x})_4$, (CZTSSe)), being an earth-abundant, highly absorbing p-type direct band gap semiconductor with an adjustable band gap[3] between ~ 1.0 - 1.5 eV, have attracted a growing attention[4] for low-cost rigid and flexible thin-film solar cells[5-11] and recently as photocathodes for efficient solar hydrogen production[12-14].

CZTSSe has been studied by various characterization techniques to improve our understanding of its structural, chemical, electronic, and thermodynamic properties[11, 15-19]. It was recognized that kesterite solar cells with off-stoichiometric composition, i.e., Cu-poor and Zn-rich, give the best PCE, with a current record of 14.9 %[2]. However, this is significantly lower than expected – the theoretical detailed balance limit[20] for a single-junction device at ~1.0 eV would be 28 %[15,21]. Other commercially available thin-film solar-cell devices (e.g., with $Cu(In,Ga)Se_2$ or CdTe absorbers) show significantly higher efficiencies[2]. The comparatively low efficiency of kesterite solar cells is mainly attributed to a large open-circuit voltage ($V_{OC}$) deficit, which could be due to the presence of defects, secondary phases, and/or the spontaneous transition from a kesterite to a stannite structure[15, 22-23]. The off-stoichiometric configuration of the kesterite structure introduces point defects such as vacancies, anti-sites, and interstitials, which significantly influence its optoelectronic properties[15, 24-25]. An optimized concentration of these defects is expected to be beneficial for enhancing the kesterite solar cell efficiency[26].

Thermal lattice excitations (phonons) play a crucial role for the thermalization and non-radiative recombination of the photo-excited charge carriers in a PV solar cell, which constitutes a fundamental limitation for achieving the radiative-limited PCEs given by thedetailed balance limit[20,-21]. The thermalization mechanism involves interactions of the hot electrons with longitudinal optical (LO) phonons, described by the Fröhlich coupling[27]. The emitted LO phonons quickly decay to acoustic phonons by Klemens[28] and/or Ridley[29] processes. Acoustic phonons, being the main heat carriers in semiconductors and insulators, exhibit large group velocities and can propagate across interfaces, which leads to an irretrievable energy loss and hence lowering the PCE of the solar cells[30].

Furthermore, the thermodynamic, elastic, and optical properties of a crystal are determined by the vibrational dynamics of the crystal lattice. A precise knowledge of the lattice dynamics is thus essential for understanding the properties of CZTSSe kesterites, including the unusually low thermal conductivity relative to other semiconductors[31], the ground-state crystal structure (kesterite, stannite, or a mixture of both)[32], and thermal expansion and electron-phonon coupling[33].

Phonon dispersion relations and element-specific phonon density of states (PDOS) of CZTSSe with various stoichiometries and crystal structures, as well as of different non-radiative recombination centers, have been extensively investigated by density functional theory (DFT)[16, 32, 34-37]. The impact of high-energy phonon states, electron-phonon coupling, and lattice anharmonicity on the PCEs have been pointed out[36-38]. Despite the comprehensive theoretical studies, experimental data on the phonon dispersions and the PDOS of real-world solar cells is missing.

The experimental determination of the lattice dynamics of solar cells under *operando* conditions (i.e., during device operation) remains a formidable challenge. Raman spectroscopy,

standardly used for structure characterization of the solar absorbers, probes only the Raman-active phonons at the center of the Brillouin zone, thus providing very limited information. Classical methods to measure the phonon dispersions in the entire Brillouin zone, such as inelastic neutron or x-ray scattering are unfeasible not only due to the small sample volume, but also because of the multi-elemental composition and multilayer structure of a thin-film solar cell. Nuclear inelastic scattering (NIS)[39-40], on the other hand, is an element- and isotope-specific method, which provides the partial PDOS of Mössbauer-active isotopes such as $^{119}$Sn (natural abundance: 8.6 %; average atomic mass of Sn: 118.71 u). The high penetration depth of x-rays with an energy of 23.88 keV, corresponding to the resonant transition[41] in the nucleus of $^{119}$Sn, combined with the sensitivity of the method to thin films[42] renders this technique ideal for investigating the lattice dynamics of Sn-containing thin-film solar cells (and other devices) with a multilayered structure.

Here, we report NIS experiments on $^{119}$Sn under dark and illuminated conditions to determine the Sn-partial PDOS as well as thermodynamic and elastic properties of CZTSSe-based thin-film solar cells with different compositions and PCEs. The results reveal variations in the phonon frequency in relation to stoichiometry variation (type and concentration of defects) and the solar cell efficiency. The formation of metastable defects is inferred from the *operando* NIS experiment of the device with the highest efficiency (10.6%). The experimentally obtained Sn-PDOS are in agreement with the results from the large body of DFT calculations in the literature[16,32,34-37].

## 2. Experimental section

**2.1. Preparation of the kesterite thin-film solar cells**: At the University of Oldenburg, the samples were prepared by a two-step process. The first step is the sputter deposition of a Cu-Sn

alloy and elemental Zn precursors on a Mo-coated soda-lime glass (SLG) substrate at room temperature. In the second step, the deposited layers were annealed in a Se- and Sn-containing atmosphere in a tube furnace at 803 K for 20 min and naturally cooled down to room temperature to obtain the CZTSe absorber with a thickness of approximately 2 μm. Afterwards, to realize solar-cell devices, a buffer layer (~ 50 nm chemical bath deposited CdS) and a transparent front contact (75 nm i-ZnO and 500 nm Al:ZnO) were sputter-deposited on top of the absorbers. For the S4 absorber, an additional rapid annealing step under $H_2S$ atmosphere was performed to exchange 25 % of the Se by S. Further details on the deposition process can be found elsewhere[10]. The compositions and achieved efficiencies of the cells are summarized in Table 1. The CZTSe absorber features a kesterite-like structure, the crystal lattice consists of alternating layers of Cu-Sn, Cu-Zn, and Cu-Sn bonds, separated by Se layers. A more detailed description of the structure is found in references[24, 32].

**Table 1.** Composition (standard deviation in parentheses) of the investigated samples, determined from energy-dispersive x-ray spectroscopy (EDX) measurements. In sample S4, 25 % of Se was replaced with S [10].

| Sample | Efficiency | Relative Composition (at. %) | | | Ratio | | |
|---|---|---|---|---|---|---|---|
| | % | Zn | Sn | Cu | Cu/(Zn+Sn) | Zn/Sn | S/(S+Se) |
| **S1** | 3.20 (0.16) | 26.16 (0.05) | 26.10 (0.15) | 47.74 (0.20) | 0.91 | 1.00 | 0 |
| **S2** | 7.60 (0.31) | 31.70 (0.66) | 24.93 (0.32) | 43.37 (0.38) | 0.76 | 1.27 | 0 |
| **S3** | 10.60 (0.33) | 33.89 (0.51) | 23.63 (0.14) | 42.47 (0.34) | 0.74 | 1.43 | 0 |
| **S4** | 4.00 (0.77) | 32.15 (0.50) | 24.95 (0.14) | 42.90 (0.41) | 0.75 | 1.29 | 0.25 |

**2.2. Nuclear inelastic scattering (NIS) experiment**: The NIS experiments at the $^{119}$Sn nuclear resonance were conducted at the High Resolution Dynamics beamline P01[43] at PETRA III (DESY, Hamburg) using x-rays with an energy of 23.88 keV. The instrumental resolution was 1.2 meV (full width at half maximum, FWHM). The three CZTSe solar cells (S1 –S3) and one

$CZTS_{0.25}Se_{0.75}$ absorber sample (S4) were illuminated at a grazing angle of 0.5° with an x-ray beam of 1.0 × 0.045 $mm^2$ (h × v). The high energy of the x-rays ensures that the entire depth of the CZTSSe layer (attenuation length of approx. 9 μm) is probed during the measurements. The measurements on all samples were conducted at 295 K. Additionally, the Sn-PDOS of sample S1 was obtained at 37 K using a helium-cooled continuous-flow cryostat.

The NIS spectra were measured in the range from –10 to +50 meV by an avalanche photodiode positioned 1 mm above the thin-film solar-cell surface (Figure S1, Supporting Information). The Sn-PDOS was obtained[44] from the experimental NIS spectra in a quasi-harmonic approximation. Sample S3 was further investigated during illumination and operation at the maximum power point (MPP = 2.7 mW, $V$ = 295 mV, $I$ = -9 mA, referred to as "*operando*"; details about the experimental setup and calculation of the "MPP" are provided in the Supporting Information), and 'open-circuit' conditions ($V_{OC}$ = 350 mV) under irradiation with two halogen cold light sources (PHILIPS, $P$ = 150 W, $T$ = 3400 K). During these measurements, the distance between the device surface and the detector was increased to allow for an efficient light irradiation, which reduced the count-rate by about a factor of three. In order to detect possible structural changes that could take place during the device operation, the Sn-PDOS of sample S3 was obtained under dark conditions before and after the *operando* and open-circuit measurements. The temperature of the sample surfaces during the dark measurements was 295(1) K. During the *operando* and open-circuit experiments, the temperature of the solar-cell surface was measured using a Lakeshore device with a Cernox® temperature sensor. The temperature of the absorber layer was determined from the detailed balance of the experimental NIS spectra measured in the range of –20 to +50 meV (Figure S2, Supporting Information). The Sn-PDOS of sample S1 at 37 K is shown in Figure S3 (Supporting Information). Raman spectra of samples S1-S3 (Figure S4, Supporting Information)

were also measured before device fabrication and are discussed in view of the composition and potential defects formation in the Supporting Information.

## 3. Results and discussion

### 3.1. Sn-PDOS from NIS measurements in the dark

The derived Sn-partial PDOS of the investigated samples are plotted in Figure 1(a). First, comparing the S-free samples with near- (sample S1) and off-stoichiometric composition (samples S2 and S3), we find similar Sn-PDOS features: two broad peaks at approx. 9 and 16 meV, the main peak at 30 meV, as well as minor states between 20 – 25 meV and 34 – 42 meV. However, a careful inspection shows distinct differences. In particular, the exact position, full width at half maximum (FWHM), and area of the peak at 30 meV vary, and the number of states (i.e., area under the PDOS curve) between 34 and 42 meV is smaller for S3 than for S1 and S2. To quantify the former effect, the peak at 30 meV was approximated by a Gaussian, shown by red solid lines in Figure 1(a), and the corresponding parameters are summarized in Table 2. For samples S2 and S3, the peak position shifts to higher energy by 1.0 and 1.1 % (i.e., by 0.29 and 0.33 meV, respectively), whereas the FWHMs increase by 24 and 32 %, respectively, compared to sample S1. The peak areas of samples S1 and S2 remain the same, while for sample S3, an increase of 6.3 % is found. This observation is in agreement with a broadening of the A2 and 230 – 250 $cm^{-1}$ Raman peaks for off-stoichiometric composition (Figure S4, right panel, Supporting Information), and is attributed to the presence of certain lattice defect types in samples S2 and S3[45-48].

To understand the experimentally derived Sn-PDOS of sample S1, it is compared with the *ab initio* calculated Sn-PDOS[32] of CZTSe with a kesterite structure (grey areas in Figure 1(a), top). This comparison unveils that the main features discussed above are reproduced by the theory, except for the phonon states between 34 – 42 meV, which are not present in the theoretically obtained Sn-PDOS.

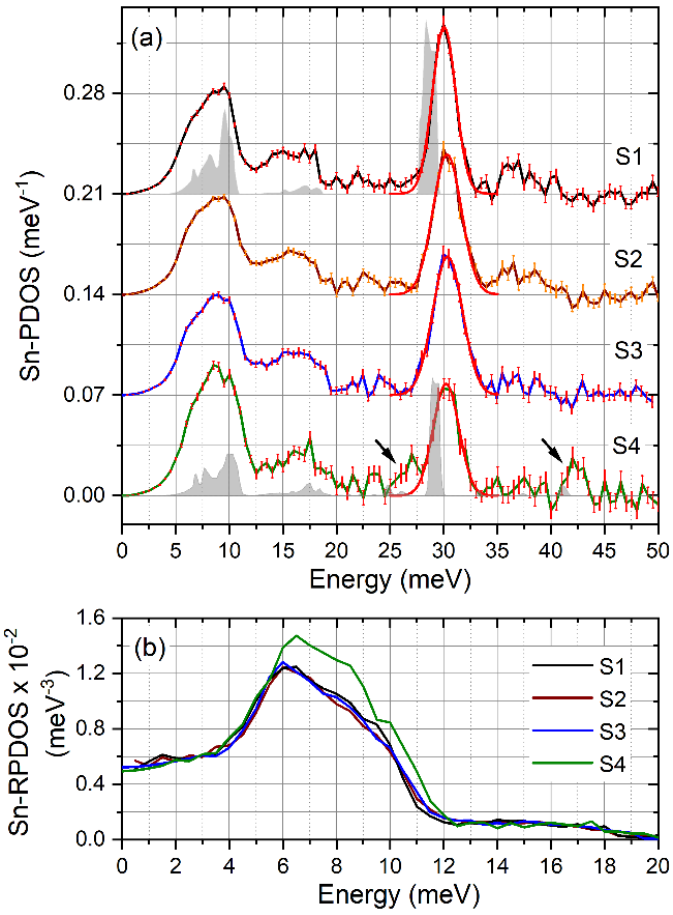


**Figure 1**. (a) Sn-PDOS and (b) reduced Sn-PDOS of the investigated samples. The curves in (a) are up-shifted by 0.07 meV$^{-1}$ for the sake of clarity. The red solid line depicts a fit of the optical mode at ~30 meV with a Gaussian (fit parameters are summarized in Table 2). The arrows in (a) point to additional peaks at ~27 and ~42.5 meV in the S-containing sample. The calculated Sn-PDOS of the kesterite crystal structures of $Cu_2ZnSnSe_4$ and $Cu_2ZnSn(S_{0.25},Se_{0.75})_4$ are shown as grey shaded areas under the experimental Sn-PDOS of S1 and S4, respectively. The calculated Sn-PDOS data is reproduced from Ref.[32] with permission from AIP Publishing.

**Table 2.** Energy, FWHM, and area of the peak at ~30 meV, as derived from the Gaussian fits in Figure 1(a).

| Sample | Energy (meV) | FWHM (meV) | Area |
|---|---|---|---|
| **S1** | 30.04(2) | 2.5(1) | 0.32(1) |
| **S2** | 30.33(2) | 3.1(1) | 0.32(1) |
| **S3** | 30.37(2) | 3.3(1) | 0.34(1) |
| **S4** | 30.23(2) | 2.9(1) | 0.23(1) |

The Sn-PDOS of the S-containing $Cu_2ZnSn(S_{0.25},Se_{0.75})_4$ absorber (sample S4, Figure 1(a), bottom) shows overall similar main features to S1 – S3, but with an increased (decreased) number of states around 9 (30) meV, additional peaks at 27 and 42.5 meV (indicated by black arrows in Figure 1(a)) and a reduced number of phonon states between 34 and 42 meV. Remarkably, the two additional peaks are predicted by the theory[32] (small grey-area peaks in Figure 1(a) bottom), with weak contributions at the lower end of the energy range of these features. The calculations[32] suggest that they originate from a coupling of Sn atoms to the vibrations of Se and S atoms.

The experimentally observed phonon states around 9 and 16 meV appear approximately at the theoretically predicted positions, whereas the peak at 30 meV is shifted by ca. 1 meV to higher energy. This shift could be attributed to a deviation of the theoretically obtained lattice constants[32, 49] from the experimental values.[50] In addition to the finite instrumental resolution, the broadening of the experimental PDOS arises from lattice defects, such as vacancies, interstitials, atomic substitutions, internal surfaces, and grain boundaries, which exist in real polycrystalline thin-film solar cells. These effects are, of course, not taken into account by the calculations performed for a stoichiometric composition and a perfect kesterite crystal structure[32].

To compare the low-energy part of the PDOS (arising primarily from the acoustic phonon modes[51]), it is convenient to plot the reduced PDOS[52] (RPDOS = PDOS*$E^{-2}$) of all samples in the energy range 0 – 20 meV (Figure 1(b)). This plot shows that, while samples S1 – S3 are very

similar, sample S4 exhibits an increased number of phonon states in the energy range 6 – 12 meV. The calculated phonon dispersions[32] reveal that, in addition to the acoustic branches, a small number of low-energy optical branches contribute to the PDOS between 6 and 12 meV. Their number is higher for the S-containing absorber, which leads to the experimentally observed difference between S1 – S3 and S4 in this energy range.

Furthermore, we discuss the experimentally observed phonon states around 16 meV and in the ranges 20 – 25 and 34 – 42 meV, which are not present in the calculated Sn-PDOS[32] (see the grey Sn-PDOS at the top of Fig. 1(a)). A careful inspection of the *ab initio* calculated Se-PDOS shows that the optical phonon states appear between 20 and 29 meV[32]. Since Sn is directly bonded to Se, one might speculate that the observed phonon states in the Sn-PDOS between 20 and 25 meV originate from vibrations of Sn coupled to those of Se atoms. In contrast, the phonon states around 14 meV and in the range 34 – 42 meV in the Sn-PDOS of CZTSe cannot be attributed to similar coupled vibrational modes. To clarify the origin of these phonon states, the Sn-PDOS of sample S1 was also obtained at 37 K. The data (Figure S3, Supporting Information) shows a significant reduction in the number of phonon states around 14 and between 34 and 42 meV. This result implies, in agreement with the *ab initio* calculations, that these phonon states do not belong to the Sn-PDOS of the CZTSe kesterite. Instead, they originate from multiphonon excitations[53], which are suppressed at lower temperatures and not fully eliminated by the data reduction algorithm[44] employed for the 295 K spectrum. This, however, does not influence our conclusions since we compare the relative changes in the Sn-PDOS of the investigated samples obtained at room temperature.

### 3.2. Investigation of defect types and secondary phases

Combined theoretical and experimental studies demonstrated that, in kesterite samples with controlled compositions, only specific defect types and secondary phases can be formed[26, 48, 54-57]. Moreover, a detailed investigation of the solar-cell efficiencies (up to 11 %, close to that of sample S3) for various absorber compositions was performed to understand the impact of the defect types[26, 58-59]. Figure 2 (left) shows a ternary composition diagram depicting the Cu-Zn-Sn contents as determined by EDX (Table 1) in atomic percentages, and Figure 2 (right) plots the cation ratio with the possible defect types depending on the composition[26, 48, 54-57, 60]. Samples S2, S3, and S4 lie in the Cu-poor, Zn-rich region (top left quadrant in the right panel of Figure 2), mainly forming defect types A ($V_{Cu} + Zn_{Cu}$) and B ($Zn_{Sn} + 2Zn_{Cu}$). Based on the composition of these samples, the formation of a ZnSe secondary phase[61-64] is expected (left panel in Figure 2). For sample S1, A and E ($V_{Cu,Zn} + Sn_{Cu,Zn}$) defect types can be expected. However, all other defect types are also likely to occur, due to the almost stoichiometric composition. These defect types are unfavorable for well-performing solar cells, since some of the defects are deep within the band gap and can act as strong recombination centers[4, 26, 35, 42-45, 59, 65]. Besides, sample S1 may also contain other binary (ZnSe, $SnSe_{2-x}$, $Cu_{2-x}Se$) and ternary ($Cu_2SnSe_3$) phases[48, 54-57, 60] (see left panel in Figure 2).

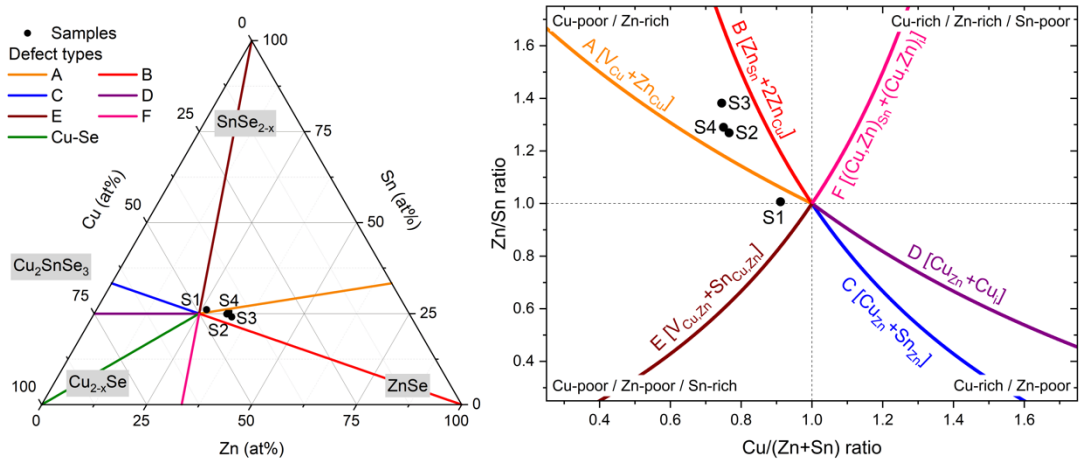

**Figure 2**. A ternary composition triangle with the possible secondary phases (left) and a cation ratio plot (right) with possible defect types[48, 54-57] for samples S1-S4 (solid black circles).

Consequently, sample S1 (i.e., the device with the lowest efficiency), might have a multitude of defect types and secondary phases. For example, $Sn_{Zn}$ and $Cu_{Zn}$+$Sn_{Zn}$ are expected to form deep carrier trap states[9, 26, 59, 65]. The $Cu_{Zn}$ + $Sn_{Zn}$ defect type could be prevalent, since the attractive interaction between the two defects could lead to a lower formation energy[66]. In addition, $Sn_{Zn}^{+2}$ and $[Cu_{Zn} + Sn_{Zn}]^{+}$ exhibit large carrier-capture cross sections, which can lead to an enhancement of the non-radiative recombination and thus reduce the PCE[36].

Furthermore, previous studies demonstrated that the defect types can affect the frequency, shape, and intensity of Raman-active modes[26, 58, 67, 68]. The mode intensity is proportional to the number of phonon states at the Γ point (center of the Brillouin zone) of respective elements and relates to the concentration of vibrating ions[26, 34, 58]. The Raman spectrum of sample S3 (Figure S4, left panel, Supporting Information) shows a reduced intensity at 173 $cm^{-1}$ (i.e., the A2 Raman mode), compared to S1 and S2. This mode mainly relates to Cu vibrations and corresponds to increased Cu vacancies ($V_{Cu}$, decreased Cu content) and the presence of $Zn_{Cu}$ anti-site defects (A-type) [26, 58, 67]. A Cu-poor and Zn-rich composition favors the formation of $Zn_{Cu}$ (increased Zn content) defects[58]. It was reported[26, 58, 67] that the presence of $Zn_{Cu}$ and $Zn_{Sn}$ anti-site defects (B-type) could give rise to intensity variations between 230 and 250 $cm^{-1}$ (Figure S4, inset left panel, Supporting Information). This observation indicates a Cu-poor and Zn-rich composition with dominating defect types A and B in sample S3, compared to S1 and S2, as discussed above (upper left quadrant in Figure 2, right panel).

The fact that the PCE remains below the theoretically predicted values indicates that other defects could be present in the bulk of the light-absorbing CZTSe layer, which is not accessible by Raman spectroscopy with its characteristic 1/e attenuation length of 50 – 60 nm, but is probed by the NIS experiment. It has recently been reported that the increased Cu-Zn disorder facilitates the formation of $Sn_{Zn}$-related defects, which are detrimental to the $V_{OC}$[69]. These defects cause a lattice distortion and shortening of the Sn – Se bond length, leading to a shift of the optical modes to higher energy[36-37,70-71]. We speculate that $Sn_{Zn}$-related defects, along with the A and B defect types discussed above, lead to the observed slight shift of the main peak at 30 meV to higher energy, as well as to an increase of its FWHM in the Sn-PDOS from S1 to S3 (Table 3).

### 3.3. Sn-PDOS from NIS measurements under illumination

Figure 3(a) shows the Sn-PDOS of S3 obtained under illuminated '*operando'* conditions (i.e., at the maximum power point, MPP) and in 'open-circuit' mode, in comparison with the Sn-PDOS obtained under 'dark' conditions 'before' and 'after' the '*operando'* measurements (see the experimental section and Supporting Information for a description of the experimental approach). Interestingly, in the Sn-PDOS, a systematic change in the position and area of the main peak at 30 meV during the "*operando*", "open-circuit", and "after" measurements is visible. In order to quantify this effect, the peak is fitted by a Gaussian profile (red lines in Figure 3(a)), and the obtained parameters are summarized in Table 3. These values show that the peak position shifts gradually to lower energy by 0.7 %, the FWHM increases by 6.1 %, and the area is reduced by 2.9 %. Similar to the Sn-PDOS of S1-S3 (Fig. 1(a)), variations of the Sn-PDOS in the energy range of 34 – 42 meV arise from multiphonon excitations are visible (see Supporting Information).

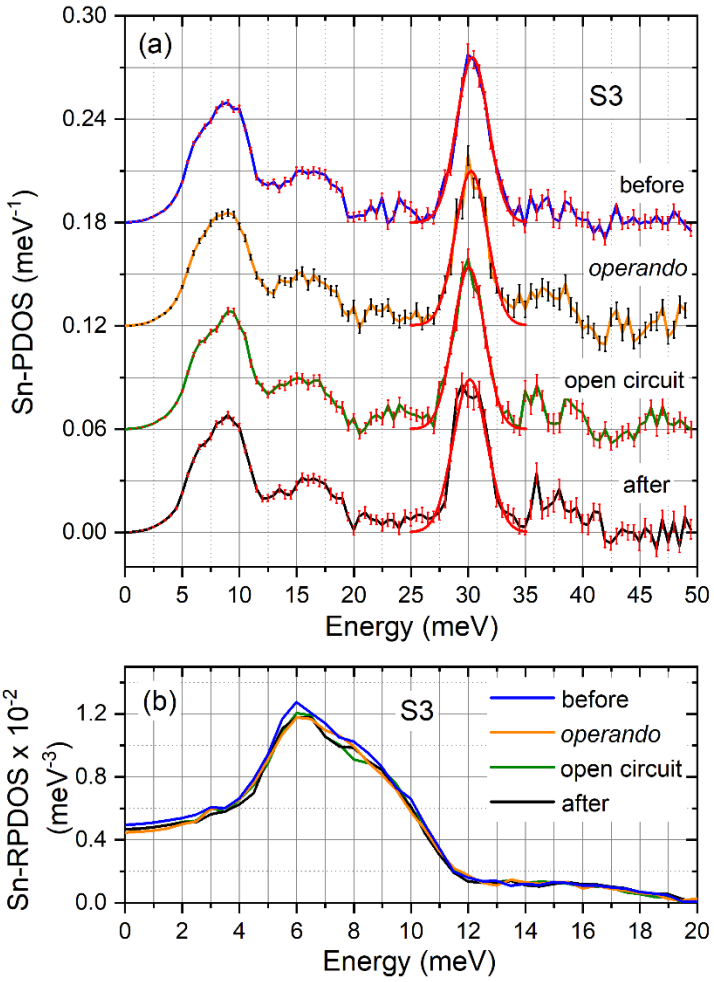


**Figure 3.** (a) Sn-PDOS and (b) reduced Sn-PDOS of the sample S3 obtained under the given experimental conditions. The curves in (a) are up-shifted by 0.06 $meV^{-1}$ for clarity. The red solid line depicts the Gaussian fit of the optical mode at ~30 meV. The obtained parameters are summarized in Table 3. The variation in the number of phonon states between 34 and 42 meV originates from multiphonon excitations (see Supporting Information).

**Table 3.** Energy, FWHM, and area of the peak at ~30 meV, as derived from the Gaussian fits in Figure 3(a).

| **S3** | **Energy (meV)** | **FWHM (meV)** | **Area** |
|---|---|---|---|
| **before** | 30.37(2) | 3.3(1) | 0.34(1) |
| ***operando*** | 30.26(3) | 3.3(1) | 0.31(1) |
| **open-circuit** | 30.06(2) | 3.3(1) | 0.32(1) |
| **after** | 30.15(4) | 3.5(1) | 0.33(1) |

It was reported that, in alloys, a red shift (lattice softening) under light illumination (particularly visible in the Sn-PDOS at 'open-circuit' mode) could be associated with an increased concentration of free charge carriers, leading to a screening between the light-generated charge carriers and the lattice ions[72-74]. Furthermore, it was reported[75-77] for Cu(In,Ga)$Se_2$ (CIGSe) and other perovskite solar cells[75] that light-soaking (blue, red, and white light illumination) and voltage bias can induce metastable defects that can trap charge carriers and lead to a lattice relaxation[75-77]. The proposed metastable defects in CIGSe are $In_{Cu}$ anti-sites, Cu interstitials, and Se vacancies in a Se-Cu divalent complex ($V_{Se}$ -$V_{Cu}$)[76-77]. For CZTSSe, an applied voltage-bias can induce $Zn^{2+}$ and $Se^{2-}$ ion migration[80]. It was also deduced that, in CZTSe, about 3 h light soaking could lead to low-energy $Cu_{Zn}$ and $V_{Cu}$ defects and a high-energy metastable defect complex ($V_{Se}$-$V_{Cu}$)[81]. A variation in the metastable defects was studied before and after AM1.5 illumination and applied bias, respectively. It was suggested that high-energy defect states, which could trap the charge carriers, are formed in the absorber during the illumination[82-83]. The metastable defects could be removed only upon heat treatment at high temperatures[83]. The open-circuit voltage after the NIS experiment remained unchanged compared to the starting value, suggesting that the general quality of the device did not degrade.

Based on these findings, we conclude that the observed changes in the Sn-PDOS of sample S3 (Figure 3(a), Table 3) after the 40 h exposure to visible light, x-rays, and applied bias originate from the formation and migration of metastable defects and/or a partial structural relaxation. The reduced Sn-PDOS (Figure 3(b)) demonstrates that the acoustic and low-energy optical phonon states remain unaffected by light irradiation and device operation.

### 3.4. Thermodynamic and elastic properties

The calculated[84] thermodynamic (vibrational entropy $S_v$, lattice specific heat capacity $C_v$) and elastic (mean square atomic displacement $< x^2>$, mean force constant $F$) properties from the experimental Sn-PDOS are summarized in Table 4. A clear trend in these parameters from sample S1 to S3 cannot be identified, except for the force constant, which reaches its lowest value in S3. This behavior, as well as the increase in $< x^2>$ and $S_v$, can be explained by the change from a near-stoichiometric composition in S1 to an off-stoichiometric composition in S3. At *operando* and open-circuit conditions, $< x^2>$ increases by 2.2 and 4.3 % (resp.), $F$ by 8.3 and 6.7 % (resp.), and $S_v$ by 2.7 % compared to the dark measurement of S3. The values of $< x^2>$ and $F$ derived at dark conditions 'after' the *operando* measurements deviate from the corresponding 'before' values by -5.4 and +11.0 %, respectively. Tentatively, this effect might be interpreted as a formation and migration of metastable defects and/or relaxation of the crystal lattice during the light irradiation.

The addition of S to CZTSe causes a further softening of the lattice. Sample S4 is characterized by the highest $< x^2>$, $S_v$, and $C_v$ (compared to the S1-S3 samples), and an $F$ value comparable to S3 (before the light irradiation). This is a consequence not only of the presence of additional phonon states at 27 and 42.5 meV, but mostly also of the enhanced number of phonon states at the low-energy part of the Sn-PDOS (Figure 1 (b)).

**Table 4.** Temperature $T$, mean square atomic displacement $<x^2>$, mean force constant $F$, vibrational entropy $S_v$, and lattice specific heat capacity at constant volume $C_v$, calculated from the Sn-PDOS of the investigated samples under the given conditions.

| **Sample** | ***T* (K)** | **$<x^2>$ (Å$^2$)** | ***F* (Nm$^{-1}$)** | **$S_v$ [3 $k_B$]** | **$C_v$ [3 $k_B$]** |
|---|---|---|---|---|---|
| **S1** | 295(1) | 0.0094(3) | 235(6) | 2.22(2) | 0.96(1) |
| **S2** | 295(1) | 0.0092(3) | 237(6) | 2.20(2) | 0.95(1) |
| **S3-before** | 295(1) | 0.0092(3) | 218(6) | 2.20(1) | 0.94(1) |

| | | | | | |
|---|---|---|---|---|---|
| **S3-*operando*** | 317(7) | 0.0094(3) | 236(6) | 2.25(2) | 0.95(1) |
| **S3-open-circuit** | 326(6) | 0.0096(3) | 233(6) | 2.27(2) | 0.95(1) |
| **S3-after** | 295(1) | 0.0087(3) | 242(7) | 2.19(2) | 0.96(1) |
| **S4** | 295(1) | 0.0104(3) | 210(8) | 2.41(2) | 1.00(1) |

From the detailed balance of the phonon annihilation and creation part of the NIS spectrum, the temperature of the light-absorbing layer during the solar cell operation can be calculated (Figure S2, Supporting Information). The derived temperatures at *operando* and open-circuit conditions, displayed in Table 4, show an increase of 22 K and 31 K, respectively, compared to the ambient temperature (295 K). The independently measured temperatures of the solar-cell surface during the *operando* (308(1) K) and open-circuit (306(1) K) experiments are lower by 9 and 20 K, respectively, than the temperature of the CZTSe absorber. This result agrees with the reported difference of approximately 10 K between the solar-cell interior and its surface, which is attributed to the difference between the light-absorption coefficients, specific heat capacities, and thermal conductivities of the top glass layer and the light-absorbing material[85].

## 4. Conclusion

In summary, we have determined the Sn-PDOS of $Cu_2ZnSnSe_4$ kesterite thin-film solar cells, with PCEs of 3.2, 7.6, and 10.6 %, using nuclear inelastic X-ray scattering on the Mössbauer-active isotope $^{119}$Sn. Although the Sn-PDOS of the three devices are similar, they exhibit distinct differences. Specifically, a systematic shift to higher energies and broadening of the most prominent peak at 30 meV is clearly detected, which is correlated to the type and concentration of defects characteristic for the investigated compositions. The Sn-PDOS of the device with the highest efficiency was additionally determined at '*operando*' and 'open-circuit' conditions. The Sn-PDOS unveils a systematic red shift (lattice softening) of the main optical phonon peak at 30

meV. A comparison of the data obtained under 'dark' conditions before and after the '*operando*' and 'open-circuit' measurements demonstrate that these variations are irreversible and suggest that structural changes have taken place. These changes are attributed to metastable defects formation, migration, and/or lattice relaxation processes as a consequence of the extended light-soaking, x-ray exposure, and/or applied bias-voltage during the solar cell operation. The temperature of the CZTSe absorber at '*operando*' and 'open-circuit' conditions was estimated from the detailed balance of the NIS spectra and was found to be higher by 9 and 20 K, respectively, than the temperature measured on the device surface. Additionally, the Sn-PDOS of $Cu_2ZnSn(S_{0.25}Se_{0.75})_4$ absorber was determined and found to exhibit features close to those of CZTSe, with additional phonon states at 27 and 42.5 meV arising from a coupling of Sn atoms to the vibrations of Se and S atoms. The experimentally obtained Sn-PDOS are in qualitative agreement with the DFT-calculated Sn-PDOS of CZTSe and CZTSSe with kesterite structure and allow for a comprehensive determination of the lattice dynamics, thermodynamic, and elastic properties of these important materials. Furthermore, this work demonstrates that advanced lattice dynamics studies, including under *operando* conditions, might contribute towards further improvement of the efficiency of kesterite-based and other thin-film solar cells for PV and PEC.

**Notes**

The authors declare no competing financial interest.

**ASSOCIATED CONTENT**

**Supporting Information**

Details of the NIS experimental setup, temperature calculation from the NIS measurements, NIS experiment at 37 K and Raman measurements and analysis.

**Acknowledgements**

*The project received funding from the European Union's Horizon 2020 research and innovation program under grant agreement No. 952982 ("Custom-Art"). D.N. thanks the Nagelschneider Stiftung for a scholarship. We thank the Manz AG and the Zentrum für Sonnenenergie- und Wasserstoff-Forschung (ZSW), Stuttgart, for providing Mo-coated soda-lime glass substrates. We acknowledge DESY (Hamburg, Germany), a member of the Helmholtz Association HGF, for the provision of experimental facilities. Parts of this research were carried out at the High Resolution Dynamics Beamline P01 at PETRA III. We thank A. Jafari, O. Leupold, C. Hagemeister, and F.-U. Dill for assistance during the experiment at P01.*

**Data Availability Statement**

The data that support the findings of this study are available from the corresponding authors upon reasonable request.

**AUTHOR INFORMATION**

Corresponding Authors

**Raju Edla*** – [a]Institute for Photon Science and Synchrotron Radiation (IPS), Karlsruhe Institute of Technology (KIT), Karlsruhe, Germany,

https://orcid.org/0000-0003-4132-8259, Email: edla.raju@kit.edu

**Svetoslav Stankov*** – [a]Institute for Photon Science and Synchrotron Radiation (IPS), Karlsruhe Institute of Technology (KIT), Karlsruhe, Germany,

[6]Laboratory for Applications of Synchrotron Radiation (LAS), Karlsruhe Institute of Technology (KIT), Karlsruhe, Germany,

https://orcid.org/0000-0002-8097-0327, Email: svetoslav.stankov@kit.edu

**Authors**

**David Nowak** - [b]Ultrafast Nanoscale Dynamics, Institute of Physics, Carl von Ossietzky University of Oldenburg, Oldenburg, Germany,

https://orcid.org/0000-0002-1456-0573, Email: david.nowak@uol.de

**Dirk Hauschild** - [a]Institute for Photon Science and Synchrotron Radiation (IPS), Karlsruhe Institute of Technology (KIT), Karlsruhe, Germany,

[c]Institute for Chemical Technology and Polymer Chemistry (ITCP), Karlsruhe Institute of Technology (KIT), Karlsruhe, Germany,

[d]Department of Chemistry and Biochemistry, University of Nevada, Las Vegas (UNLV), Las Vegas, NV, USA,

https://orcid.org/0000-0001-9088-8944, Email: dirk.hauschild@kit.edu

**Ilya Sergueev** - [e]Deutsches Elektronen-Synchrotron DESY, Hamburg, Germany,

https://orcid.org/0000-0002-7614-2238, Email: ilya.sergeev@desy.de

**Devendra Pareek** - [b]Ultrafast Nanoscale Dynamics, Institute of Physics, Carl von Ossietzky University of Oldenburg, Oldenburg, Germany,

https://orcid.org/0000-0001-7231-6686, Email: Devendra.pareek@uol.de

**Levent Gütay** - [b]Ultrafast Nanoscale Dynamics, Institute of Physics, Carl von Ossietzky University of Oldenburg, Oldenburg, Germany,

https://orcid.org/0000-0002-7626-8586, Email: levent.guetay@uol.de

**Clemens Heske** - [a]Institute for Photon Science and Synchrotron Radiation (IPS), Karlsruhe Institute of Technology (KIT), Karlsruhe, Germany,

[c]Institute for Chemical Technology and Polymer Chemistry (ITCP), Karlsruhe Institute of Technology (KIT), Karlsruhe, Germany,

[d]Department of Chemistry and Biochemistry, University of Nevada, Las Vegas (UNLV), Las Vegas, NV, USA,

https://orcid.org/0000-0001-7586-4549, Email: heske@kit.edu

**Lothar Weinhardt** - [a]Institute for Photon Science and Synchrotron Radiation (IPS), Karlsruhe Institute of Technology (KIT), Karlsruhe, Germany,

[c]Institute for Chemical Technology and Polymer Chemistry (ITCP), Karlsruhe Institute of Technology (KIT), Karlsruhe, Germany,

[d]Department of Chemistry and Biochemistry, University of Nevada, Las Vegas (UNLV), Las Vegas, NV, USA,

https://orcid.org/0000-0003-3361-1054, Email: lothar.weinhardt@kit.edu

## REFERENCES

(1) Lv, J.; Xie, J.; Mohamed, A. G. A.; Zhang, X.; Feng, Y.; Jiao, L.; Zhou, E.; Yuan, D.; Wang, Y. Solar utilization beyond photosynthesis. *Nature Reviews Chemistry* **2023**, *7* (2), 91-105. DOI: 10.1038/s41570-022-00448-9.

(2) National Renewable Energy Laboratory. *Research Cell Efficiency Records. Available online: https://www.nrel.gov/pv/assets/pdfs/best-research-cell-efficiencies.pdf, (accessed on 25 March 2024)*.

(3) Yang, K.-J.; Son, D.-H.; Sung, S.-J.; Sim, J.-H.; Kim, Y.-I.; Park, S.-N.; Jeon, D.-H.; Kim, J.; Hwang, D.-K.; Jeon, C.-W.; et al. A band-gap-graded CZTSSe solar cell with 12.3% efficiency. *Journal of Materials Chemistry A* **2016**, *4* (26), 10151-10158. DOI: 10.1039/C6TA01558A.
(4) Wang, A.; He, M.; Green, M. A.; Sun, K.; Hao, X. A Critical Review on the Progress of Kesterite Solar Cells: Current Strategies and Insights. *Advanced Energy Materials* **2023**, *13* (2), 2203046. DOI: https://doi.org/10.1002/aenm.202203046.
(5) Li, J.; Sun, K.; Yuan, X.; Huang, J.; Green, M. A.; Hao, X. Emergence of flexible kesterite solar cells: progress and perspectives. *npj Flexible Electronics* **2023**, *7* (1), 16. DOI: 10.1038/s41528-023-00250-7.
(6) Pan, X.; Li, X.; Yang, Y.; Xiang, C.; Xu, A.; Liu, H.; Yan, W.; Huang, W.; Xin, H. 12.3% Efficient Low Voc Loss Pure Sulfide Kesterite Solar Cells from DMSO Solution via Cadmium Alloying. *Advanced Energy Materials* **2023**, *13* (38), 2301780. DOI: https://doi.org/10.1002/aenm.202301780.
(7) Zhou, Y.; Xiang, C.; Dai, Q.; Xiang, S.; Li, R.; Gong, Y.; Zhu, Q.; Yan, W.; Huang, W.; Xin, H. 11.4% Efficiency Kesterite Solar Cells on Transparent Electrode. *Advanced Energy Materials* **2023**, *13* (19), 2300253. DOI: https://doi.org/10.1002/aenm.202300253.
(8) Yu, Z.; Li, C.; Chen, S.; Zheng, Z.; Fan, P.; Li, Y.; Tan, M.; Yan, C.; Zhang, X.; Su, Z.; Liang G. Unveiling the Selenization Reaction Mechanisms in Ambient Air-Processed Highly Efficient Kesterite Solar Cells. *Advanced Energy Materials* **2023**, *13* (19), 2300521. DOI: https://doi.org/10.1002/aenm.202300521.
(9) Otgontamir, N.; Enkhbat, T.; Enkhbayar, E.; Song, S.; Kim, S. Y.; Hong, T. E.; Kim, J. High Efficiency Kesterite Solar Cells Through a Dual Treatment Approach: Improving the Quality of both Absorber Bulk and Heterojunction Interface. *Advanced Energy Materials* **2023**, *13*(14), 2302941. DOI: https://doi.org/10.1002/aenm.202302941.
(10) Taskesen, T.; Pareek, D.; Hauschild, D.; Haertel, A.; Weinhardt, L.; Yang, W.; Pfeiffelmann, T.; Nowak, D.; Heske, C.; Gütay, L. Steep sulfur gradient in CZTSSe solar cells by $H_2S$-assisted rapid surface sulfurization. *RSC Advances* **2021**, *11* (21), 12687-12695, DOI: 10.1039/D1RA00494H.
(11) Taskesen, T.; Steininger, V.; Chen, W.; Ohland, J.; Mikolajczak, U.; Pareek, D.; Parisi, J.; Gütay, L. Resilient and reproducible processing for CZTSe solar cells in the range of 10%. *Progress in Photovoltaics: Research and Applications* **2018**, *26* (12), 1003-1006. DOI: https://doi.org/10.1002/pip.3063.
(12) Kumar, M.; Meena, B.; Subramanyam, P.; Suryakala, D.; Subrahmanyam, C. Recent trends in photoelectrochemical water splitting: the role of cocatalysts. *NPG Asia Materials* **2022**, *14* (1), 88. DOI: 10.1038/s41427-022-00436-x.
(13) Liang, G.; Li, Z.; Ishaq, M.; Zheng, Z.; Su, Z.; Ma, H.; Zhang, X.; Fan, P.; Chen, S. Charge Separation Enhancement Enables Record Photocurrent Density in $Cu_2ZnSn(S,Se)_4$ Photocathodes for Efficient Solar Hydrogen Production. *Advanced Energy Materials* **2023**, *13* (19), 2300215. DOI: https://doi.org/10.1002/aenm.202300215.
(14) Huang, D.; Wang, K.; Li, L.; Feng, K.; An, N.; Ikeda, S.; Kuang, Y.; Ng, Y.; Jiang, F. 3.17% efficient $Cu_2ZnSnS_4$–$BiVO_4$ integrated tandem cell for standalone overall solar water splitting. *Energy & Environmental Science* **2021**, *14* (3), 1480-1489, DOI: 10.1039/D0EE03892J.
(15) Wallace, S. K.; Mitzi, D. B.; Walsh, A. The Steady Rise of Kesterite Solar Cells. *ACS Energy Letters* **2017**, *2* (4), 776-779. DOI: 10.1021/acsenergylett.7b00131.
(16) Khare, A.; Himmetoglu, B.; Johnson, M.; Norris, D. J.; Cococcioni, M.; Aydil, E. S. Calculation of the lattice dynamics and Raman spectra of copper zinc tin chalcogenides and

comparison to experiments. *Journal of Applied Physics* **2012**, *111* (8), 083707. DOI: 10.1063/1.4704191.
(17) Hauschild, D.; Wachs, S. J.; Kogler, W.; Seitz, L.; Carter, J.; Schnabel, T.; Krause, B.; Blum, M.; Yang, W.; Ahlswede, E.; et al. Chemical Structure of a Carbon-Rich Layer at the Wet-Chemical Processed $Cu_2ZnSn(S,Se)_4$/Mo Interface. *IEEE Journal of Photovoltaics* **2021**, *11* (3), 658-663. DOI: 10.1109/JPHOTOV.2021.3059423.
(18) Kogler, W.; Schnabel, T.; Ahlswede, E.; Taskesen, T.; Gütay, L.; Hauschild, D.; Weinhardt, L.; Heske, C.; Seeger, J.; Hetterich, M.; M. Powalla. Hybrid chemical bath deposition-CdS/sputter-Zn(O,S) alternative buffer for $Cu_2ZnSn(S,Se)_4$ based solar cells. *Journal of Applied Physics* **2020**, *127* (16), 165301-165309. DOI: 10.1063/1.5142550.
(19) Chen, W.; Taskesen, T.; Nowak, D.; Mikolajczak, U.; Sayed, M. H.; Pareek, D.; Ohland, J.; Schnabel, T.; Ahlswede, E.; Hauschild, D.; et al. Modifications of the CZTSe/Mo back-contact interface by plasma treatments. *RSC Advances* **2019**, *9* (46), 26850-26855, DOI: 10.1039/C9RA02847A.
(20) Shockley, W.; Queisser, H. J. Detailed Balance Limit of Efficiency of p-n Junction Solar Cells. *Journal of Applied Physics* **2004**, *32* (3), 510-519. DOI: 10.1063/1.1736034.
(21) Luo, D.; Su, R.; Zhang, W.; Gong, Q.; Zhu, R. Minimizing non-radiative recombination losses in perovskite solar cells. *Nature Reviews Materials* **2020**, *5* (1), 44-60. DOI: 10.1038/s41578-019-0151-y.
(22) Gong, Y.; Zhang, Y.; Zhu, Q.; Zhou, Y.; Qiu, R.; Niu, C.; Yan, W.; Huang, W.; Xin, H. Identifying the origin of the $V_{OC}$ deficit of kesterite solar cells from the two grain growth mechanisms induced by $Sn^{2+}$ and $Sn^{4+}$ precursors in DMSO solution. *Energy & Environmental Science* **2021**, *14* (4), 2369-2380, DOI: 10.1039/D0EE03702H.
(23) Siebentritt, S.; Schorr, S. Kesterites - a challenging material for solar cells. *Progress in Photovoltaics: Research and Applications* **2012**, *20* (5), 512-519. DOI: https://doi.org/10.1002/pip.2156.
(24) Schorr, S.; Gurieva, G.; Guc, M.; Dimitrievska, M.; Pérez-Rodríguez, A.; Izquierdo-Roca, V.; Schnohr, C. S.; Kim, J.; Jo, W.; Merino, J. M. Point defects, compositional fluctuations, and secondary phases in non-stoichiometric kesterites. *Journal of Physics: Energy* **2019**, *2* (1), 012002. DOI: 10.1088/2515-7655/ab4a25.
(25) Rudisch, K.; Davydova, A.; Platzer-Björkman, C.; Scragg, J. The effect of stoichiometry on Cu-Zn ordering kinetics in $Cu_2ZnSnS_4$ thin films. *Journal of Applied Physics* **2018**, *123* (16), 161558. DOI: 10.1063/1.5010081.
(26) Dimitrievska, M.; Oliva, F.; Guc, M.; Giraldo, S.; Saucedo, E.; Pérez-Rodríguez, A.; Izquierdo-Roca, V. Defect characterisation in $Cu_2ZnSnSe_4$ kesterites via resonance Raman spectroscopy and the impact on optoelectronic solar cell properties. *Journal of Materials Chemistry A* **2019**, *7* (21), 13293-13304, DOI: 10.1039/C9TA03625C.
(27) Fröhlich, H. Electrons in lattice fields. *Advances in Physics* **1954**, *3* (11), 325-361. DOI: 10.1080/00018735400101213.
(28) Klemens, P. G. Anharmonic Decay of Optical Phonons. *Physical Review* **1966**, *148* (2), 845-848. DOI: 10.1103/PhysRev.148.845.
(29) Ridley, B. K. Electron scattering by confined LO polar phonons in a quantum well. *Physical Review B* **1989**, *39* (8), 5282-5286. DOI: 10.1103/PhysRevB.39.5282.
(30) Othonos, A. Probing ultrafast carrier and phonon dynamics in semiconductors. *Journal of Applied Physics* **1998**, *83* (4), 1789-1830. DOI: 10.1063/1.367411.

(31) Zhu, Y.; Liu, Y.; Ren, G.; Tan, X.; Yu, M.; Lin, Y.-H.; Nan, C.-W.; Marcelli, A.; Hu, T.; Xu, W. Lattice Dynamics and Thermal Conductivity in $Cu_2Zn_{1-x}Co_xSnSe_4$. *Inorganic Chemistry* **2018**, *57* (10), 6051-6056. DOI: 10.1021/acs.inorgchem.8b00569.
(32) Khare, A.; Himmetoglu, B.; Cococcioni, M.; Aydil, E. S. First principles calculation of the electronic properties and lattice dynamics of $Cu_2ZnSn(S_{1-x}Se_x)_4$. *Journal of Applied Physics* **2012**, *111* (12), 123704. DOI: 10.1063/1.4728232.
(33) Monserrat, B.; Park, J.-S.; Kim, S.; Walsh, A. Role of electron-phonon coupling and thermal expansion on band gaps, carrier mobility, and interfacial offsets in kesterite thin-film solar cells. *Applied Physics Letters* **2018**, *112* (19), 193903. DOI: 10.1063/1.5028186.
(34) Mortazavi Amiri, N. B.; Postnikov, A. Electronic structure and lattice dynamics in kesterite-type $Cu_2ZnSnSe_4$ from first-principles calculations. *Physical Review B* **2010**, *82* (20), 205204. DOI: 10.1103/PhysRevB.82.205204.
(35) Gürel, T.; Sevik, C.; Çağın, T. Characterization of vibrational and mechanical properties of quaternary compounds $Cu_2ZnSnS_4$ and $Cu_2ZnSnSe_4$ in kesterite and stannite structures. *Physical Review B* **2011**, *84* (20), 205201. DOI: 10.1103/PhysRevB.84.205201.
(36) Li, J.; Yuan, Z.-K.; Chen, S.; Gong, X.-G.; Wei, S.-H. Effective and Noneffective Recombination Center Defects in $Cu_2ZnSnS_4$: Significant Difference in Carrier Capture Cross Sections. *Chemistry of Materials* **2019**, *31* (3), 826-833. DOI: 10.1021/acs.chemmater.8b03933.
(37) Xu, Y.; Yang, J.-H.; Chen, S.; Gong, X.-G. Defect-assisted nonradiative recombination in $Cu_2ZnSnSe_4$: A comparative study with $Cu_2ZnSnSe_4$. *Physical Review Materials* **2021**, *5* (2), 025403. DOI: 10.1103/PhysRevMaterials.5.025403.
(38) Zhang, P.; Hou, Z.; Jiang, L.; Yang, J.; Saidi, W. A.; Prezhdo, O. V.; Li, W. Weak Anharmonicity Rationalizes the Temperature-Driven Acceleration of Nonradiative Dynamics in $Cu_2ZnSnS_4$ Photoabsorbers. *ACS Applied Materials & Interfaces* **2021**, *13* (51), 61365-61373. DOI: 10.1021/acsami.1c21526.
(39) Seto, M.; Yoda, Y.; Kikuta, S.; Zhang, X. W.; Ando, M. Observation of Nuclear Resonant Scattering Accompanied by Phonon Excitation Using Synchrotron Radiation. *Physical Review Letters* **1995**, *74* (19), 3828-3831. DOI: 10.1103/PhysRevLett.74.3828.
(40) Sturhahn, W.; Toellner, T. S.; Alp, E. E.; Zhang, X.; Ando, M.; Yoda, Y.; Kikuta, S.; Seto, M.; Kimball, C. W.; Dabrowski, B. Phonon Density of States Measured by Inelastic Nuclear Resonant Scattering. *Physical Review Letters* **1995**, *74* (19), 3832-3835. DOI: 10.1103/PhysRevLett.74.3832.
(41) Chumakov, A. I.; Barla, A.; Rüffer, R.; Metge, J.; Grünsteudel, H. F.; Grünsteudel, H.; Plessel, J.; Winkelmann, H.; Abd-Elmeguid, M. M. Nuclear inelastic scattering of synchrotron radiation by $^{119}$Sn. *Physical Review B* **1998**, *58* (1), 254-257. DOI: 10.1103/PhysRevB.58.254.
(42) Stankov, S.; Röhlsberger, R.; Ślęzak, T.; Sladecek, M.; Sepiol, B.; Vogl, G.; Chumakov, A. I.; Rüffer, R.; Spiridis, N.; Łażewski, J.; et al. Phonons in Iron: From the Bulk to an Epitaxial Monolayer. *Physical Review Letters* **2007**, *99* (18), 185501. DOI: 10.1103/PhysRevLett.99.185501.
(43) Wille, H. C.; Franz, H.; Röhlsberger, R.; Caliebe, W. A.; Dill, F. U. Nuclear resonant scattering at PETRA III : Brillant opportunities for nano – and extreme condition science. *Journal of Physics: Conference Series* **2010**, *217*, 012008. DOI: 10.1088/1742-6596/217/1/012008.
(44) Kohn, V. G.; Chumakov, A. I. DOS: Evaluation of phonon density of states from nuclear resonant inelastic absorption. *Hyperfine Interactions* **2000**, *125* (1), 205-221. DOI: 10.1023/A:1012689705503.

(45) Xu, B.; Qin, X.; Lin, J.; Chen, J.; Tong, H.; Qi, R.; Yue, F.; Chen, Y.; Yang, P.; Chu, J.; et al. Positive Role of Inhibiting CZTSSe Decomposition on Intrinsic Defects and Interface Recombination of 12.03% Efficient Kesterite Solar Cells. *Solar RRL* **2022**, *6* (8), 2200256. DOI: https://doi.org/10.1002/solr.202200256.
(46) Dimitrievska, M.; Fairbrother, A.; Pérez-Rodríguez, A.; Saucedo, E.; Izquierdo-Roca, V. Raman scattering crystalline assessment of polycrystalline $Cu_2ZnSnS_4$ thin films for sustainable photovoltaic technologies: Phonon confinement model. *Acta Materialia* **2014**, *70*, 272-280. DOI: https://doi.org/10.1016/j.actamat.2014.02.035.
(47) Rey, G.; Redinger, A.; Sendler, J.; Weiss, T. P.; Thevenin, M.; Guennou, M.; Adib, B. E.; Siebentritt, S. The band gap of $Cu_2ZnSnSe_4$: Effect of order-disorder. *Applied Physics Letters* **2014**, *105* (11), 112106. DOI: 10.1063/1.4896315.
(48) Gershon, T.; Gokmen, T.; Gunawan, O.; Haight, R.; Guha, S.; Shin, B. Understanding the relationship between $Cu_2ZnSn(S,Se)_4$ material properties and device performance. *MRS Communications* **2014**, *4* (4), 159-170. DOI: 10.1557/mrc.2014.34.
(49) Suresh Babu, G.; Kishore Kumar, Y. B.; Uday Bhaskar, P.; Sundara Raja, V. Growth and characterization of co-evaporated $Cu_2ZnSnSe_4$ thin films for photovoltaic applications. *Journal of Physics D: Applied Physics* **2008**, *41* (20), 205305. DOI: 10.1088/0022-3727/41/20/205305.
(50) Tong, C.-J.; Edwards, H. J.; Hobson, T. D. C.; Durose, K.; Dhanak, V. R.; Major, J. D.; McKenna, K. P. Density Functional Theory and Experimental Determination of Band Gaps and Lattice Parameters in Kesterite $Cu_2ZnSn(S_xSe_{1-x})_4$. *The Journal of Physical Chemistry Letters* **2020**, *11* (24), 10463-10468. DOI: 10.1021/acs.jpclett.0c03205.
(51) Kittel, C. Introduction to solid state physics (8th ed.). *Wiley: Newyork,* **2004**.
(52) Chumakov, A. I.; Monaco, G.; Monaco, A.; Crichton, W. A.; Bosak, A.; Rüffer, R.; Meyer, A.; Kargl, F.; Comez, L.; Fioretto, D.; et al. Equivalence of the Boson Peak in Glasses to the Transverse Acoustic van Hove Singularity in Crystals. *Physical Review Letters* **2011**, *106* (22), 225501. DOI: 10.1103/PhysRevLett.106.225501.
(53) Chumakov, A. I.; Sturhahn, W. Experimental aspects of inelastic nuclear resonance scattering. *Hyperfine Interactions* **1999**, *123* (1), 781-808. DOI: 10.1023/A:1017052730094.
(54) Lafond, A.; Choubrac, L.; Guillot-Deudon, C.; Deniard, P.; Jobic, S. Crystal Structures of Photovoltaic Chalcogenides, an Intricate Puzzle to Solve: the Cases of CIGSe and CZTS Materials. *Zeitschrift für anorganische und allgemeine Chemie* **2012**, *638* (15), 2571-2577. DOI: https://doi.org/10.1002/zaac.201200279.
(55) Olekseyuk, I. D.; Dudchak, I. V.; Piskach, L. V. Phase equilibria in the $Cu_2S$–$ZnS$–$SnS_2$ system. *Journal of Alloys and Compounds* **2004**, *368* (1), 135-143. DOI: https://doi.org/10.1016/j.jallcom.2003.08.084.
(56) Gurieva, G.; Dimitrievska, M.; Zander, S.; Pérez-Rodríguez, A.; Izquierdo-Roca, V.; Schorr, S. Structural characterisation of $Cu_{2.04}Zn_{0.91}Sn_{1.05}S_{2.08}Se_{1.92}$. *physica status solidi c* **2015**, *12* (6), 588-591. DOI: https://doi.org/10.1002/pssc.201400307.
(57) Chen, S.; Yang, J.-H.; Gong, X. G.; Walsh, A.; Wei, S.-H. Intrinsic point defects and complexes in the quaternary kesterite semiconductor $Cu_2ZnSnS_4$. *Physical Review B* **2010**, *81* (24), 245204. DOI: 10.1103/PhysRevB.81.245204.
(58) Dimitrievska, M.; Fairbrother, A.; Saucedo, E.; Pérez-Rodríguez, A.; Izquierdo-Roca, V. Influence of compositionally induced defects on the vibrational properties of device grade $Cu_2ZnSnSe_4$ absorbers for kesterite based solar cells. *Applied Physics Letters* **2015**, *106* (7), 073903. DOI: 10.1063/1.4913262.

(59) Kumar, M.; Dubey, A.; Adhikari, N.; Venkatesan, S.; Qiao, Q. Strategic review of secondary phases, defects and defect-complexes in kesterite CZTS–Se solar cells. *Energy & Environmental Science* **2015**, *8* (11), 3134-3159, DOI: 10.1039/C5EE02153G.
(60) Bourdais, S.; Choné, C.; Delatouche, B.; Jacob, A.; Larramona, G.; Moisan, C.; Lafond, A.; Donatini, F.; Rey, G.; Siebentritt, S.; et al. Is the Cu/Zn Disorder the Main Culprit for the Voltage Deficit in Kesterite Solar Cells? *Advanced Energy Materials* **2016**, *6* (12), 1502276. DOI: https://doi.org/10.1002/aenm.201502276.
(601) Ruiz-Perona, A.; Sánchez, Y.; Guc, M.; Calvo-Barrio, L.; Jawhari, T.; Merino, J. M.; León, M.; Caballero, R. Influence of Zn excess on compositional, structural and vibrational properties of $Cu_2ZnSn_{0.5}Ge_{0.5}Se_4$ thin films and their effect on solar cell efficiency. *Solar Energy* **2020**, *199*, 864-871. DOI: https://doi.org/10.1016/j.solener.2020.02.082.
(62) Stanchik, A. V.; Tivanov, M. S.; Tyukhov, I. I.; Juskenas, R.; Korolik, O. V.; Gremenok, V. F.; Saad, A. M.; Naujokaitis, A. Temperature dependence of Raman scattering in the $Cu_2ZnSnSe_4$ thin films on a Ta foil substrate. *Solar Energy* **2020**, *201*, 480-488. DOI: https://doi.org/10.1016/j.solener.2020.03.043.
(63) Gurieva, G.; Levcenco, S.; Pereira Correia de Sousa, A.; Unold, T.; Schorr, S. Investigation of Detection Limits of ZnSe and $Cu_2SnSe_3$ Secondary Phases in $Cu_2ZnSnSe_4$. *physica status solidi c* **2017**, *14* (10), 1700166. DOI: https://doi.org/10.1002/pssc.201700166.
(64) López-Marino, S.; Sánchez, Y.; Placidi, M.; Fairbrother, A.; Espindola-Rodríguez, M.; Fontané, X.; Izquierdo-Roca, V.; López-García, J.; Calvo-Barrio, L.; Pérez-Rodríguez, A.; Saucedo, E. ZnSe Etching of Zn-Rich $Cu_2ZnSnSe_4$: An Oxidation Route for Improved Solar-Cell Efficiency. *Chemistry – A European Journal* **2013**, *19* (44), 14814-14822. DOI: https://doi.org/10.1002/chem.201302589.
(65) Tiwari, D.; Yakushev, M. V.; Koehler, T.; Cattelan, M.; Fox, N.; Martin, R. W.; Klenk, R.; Férmin, D. J. Mapping the Energetics of Defect States in $Cu_2ZnSnS_4$ films and the Impact of Sb Doping. *ACS Applied Energy Materials* **2022**, *5* (4), 3933-3940. DOI: 10.1021/acsaem.1c03729.
(66) Chen, S.; Wang, L.-W.; Walsh, A.; Gong, X. G.; Wei, S.-H. Abundance of $Cu_{Zn} + Sn_{Zn}$ and $2Cu_{Zn} + Sn_{Zn}$ defect clusters in kesterite solar cells. *Applied Physics Letters* **2012**, *101* (22), 223901 -223904. DOI: 10.1063/1.4768215.
(67) Nowak, D.; Atlan, F.; Pareek, D.; Guc, M.; Perez-Rodriguez, A.; Izquierdo-Roca, V.; Gütay, L. Influence of the precursor composition on the resulting absorber properties and defect concentration in $Cu_2ZnSnSe_4$ absorbers. *Solar Energy Materials and Solar Cells* **2023**, *256*, 112342. DOI: https://doi.org/10.1016/j.solmat.2023.112342.
(68) Dimitrievska, M.; Giraldo, S.; Pistor, P.; Saucedo, E.; Pérez-Rodríguez, A.; Izquierdo-Roca, V. Raman scattering analysis of the surface chemistry of kesterites: Impact of post-deposition annealing and Cu/Zn reordering on solar cell performance. *Solar Energy Materials and Solar Cells* **2016**, *157*, 462-467. DOI: https://doi.org/10.1016/j.solmat.2016.07.009.
(69) Chen W.; Dahliah, D:, Rignanese, G. -M.; Hautier, G. Origin of the Low Conversion Efficiency in $Cu_2ZnSnS_4$ Kesterite Solar Cells: The Actual Role of Cation Disorder. *Energy & Environmental Science* **2021**, *14*, 3567-3578. DOI: 10.1039/D1EE00260K
(70) Kim, S.; Park, J.-S.; Hood, Samantha N.; Walsh, A., Lone-Pair Effect on Carrier Capture in $Cu_2ZnSnS_4$ Solar Cells. *Journal of Materials Chemistry A* **2019**, *7*, 2686-2693. DOI: 10.1039/C8TA10130B.
(71) Persson, C., Electronic and optical properties of $Cu_2ZnSnS_4$ and $Cu_2ZnSnSe_4$. *Journal of Applied Physics* **2010,** *107* (5), 053710-053717. DOI: 10.1063/1.3318468

(72) Delaire, O.; Marty, K.; Stone, M. B.; Kent, P. R. C.; Lucas, M. S.; Abernathy, D. L.; Mandrus, D.; Sales, B. C. Phonon softening and metallization of a narrow-gap semiconductor by thermal disorder. *Proceedings of the National Academy of Sciences* **2011**, *108* (12), 4725-4730. DOI: doi:10.1073/pnas.1014869108.
(73) Bragaglia, V.; Ramsteiner, M.; Schick, D.; Boschker, J. E.; Mitzner, R.; Calarco, R.; Holldack, K. Phonon anharmonicities and ultrafast dynamics in epitaxial $Sb_2Te_3$. *Scientific Reports* **2020**, *10* (1), 12962. DOI: 10.1038/s41598-020-69663-y.
(74) Zhang, B.; Chang, R.; Wang, K.; Lü, J.-T.; Wang, S. Optical Phonon Behaviors of Photocharged Nanocrystals: Effects of Free Charge Carriers. *The Journal of Physical Chemistry Letters* **2018**, *9* (17), 5055-5062. DOI: 10.1021/acs.jpclett.8b01831.
(75) Meyer, T.; Engelhardt, F.; Parisi, J.; Rau, U. Spectral dependence and Hall effect of persistent photoconductivity in polycrystalline $Cu(In,Ga)Se_2$ thin films. *Journal of Applied Physics* **2002**, *91* (8), 5093-5099. DOI: 10.1063/1.1459597.
(76) Lany, S.; Zunger, A. Light- and bias-induced metastabilities in $Cu(In,Ga)Se_2$ based solar cells caused by the ($V_{Se}$-$V_{Cu}$) vacancy complex. *Journal of Applied Physics* **2006**, *100* (11). DOI: 10.1063/1.2388256.
(77) Rau, U.; Schmitt, M.; Parisi, J.; Riedl, W.; Karg, F. Persistent photoconductivity in $Cu(In,Ga)Se_2$ heterojunctions and thin films prepared by sequential deposition. *Applied Physics Letters* **1998**, *73* (2), 223-225. DOI: 10.1063/1.121762.
(78) Tsai, H.; Asadpour, R.; Blancon, J.-C.; Stoumpos, C. C.; Durand, O.; Strzalka, J. W.; Chen, B.; Verduzco, R.; Ajayan, P. M.; Tretiak, S.; et al. Light-induced lattice expansion leads to high-efficiency perovskite solar cells. *Science* **2018**, *360* (6384), 67-70. DOI: doi:10.1126/science.aap8671.
(79) Lang, D. V.; Logan, R. A. Large-Lattice-Relaxation Model for Persistent Photoconductivity in Compound Semiconductors. *Physical Review Letters* **1977**, *39* (10), 635-639. DOI: 10.1103/PhysRevLett.39.635.
(80) O'Neill, A.; Jo, E.; Choi, E.; Park, J.; Kim, J. H.; Yun, J. S.; Seidel, J. Enhancing CZTSSe solar cells through electric field induced ion migration. *Journal of Materials Chemistry A* **2022**, *10* (10), 5642-5649, DOI: 10.1039/D1TA10638D.
(81) Lloyd, M. A.; Kuba, A. G.; McCandless, B. E.; Birkmire, R. Admittance spectroscopy on single-crystal $Cu_2ZnSnSe_4$ solar cells: Back-contact effects and metastabilities. *Journal of Applied Physics* **2020**, *128* (14), 143102 - 143113. DOI: 10.1063/5.0020421.
(82) Koeper, M. J.; Hages, C. J.; Li, J. V.; Levi, D.; Agrawal, R. Metastable defect response in CZTSSe from admittance spectroscopy. *Applied Physics Letters* **2017**, *111* (14), 142105 - 142108. DOI: 10.1063/1.4996283.
(83) Lyam, M. S.; Hölscher, T.; Maiberg, M.; Cabas-Vidani, A.; Hernandez-Martinez, A.; Tampo, H.; Scheer, R. Dominant recombination path in low-bandgap kesterite CZTSe(S) solar cells from red light induced metastability. *Journal of Applied Physics* **2021**, *129* (20), 205703 - 205722. DOI: 10.1063/5.0045324.
(84) Hu, M. Y.; Toellner, T. S.; Dauphas, N.; Alp, E. E.; Zhao, J. Moments in nuclear resonant inelastic x-ray scattering and their applications. *Physical Review B* **2013**, *87* (6), 064301 - 064313. DOI: 10.1103/PhysRevB.87.064301.
(85) Rahman, M. M.; Hasanuzzaman, M.; Rahim, N. A. Effects of various parameters on PV-module power and efficiency. *Energy Conversion and Management* **2015**, *103*, 348-358. DOI: https://doi.org/10.1016/j.enconman.2015.06.067

## TOC Graphic

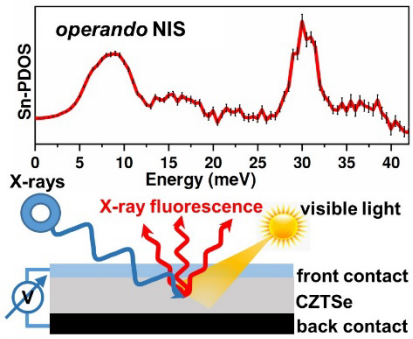
operando NIS
Sn-PDOS
0 5 10 15 20 25 30 35 40
Energy (meV)
X-rays
X-ray fluorescence
visible light
V
front contact
CZTSe
back contact